Title

Compositionally Complex Spinel Oxides as Conversion Anodes for Lithium-Ion Batteries.

Authors

Nam, Ki-Hun
Wang, Zhongling
Luo, Jessica
et al.

Publication Date

2025-04-07

DOI

10.1021/acsami.4c21332

Compositionally Complex Spinel Oxides as Conversion Anodes for Lithium-Ion Batteries

Ki-Hun Nam,[a] Zhongling Wang,[f, h] Jessica Luo,[f, g] Juhyeon Ahn,[a] Zachary R. Mansley,[i]
Seungkyu Kim,[b,c,d] Myoung Hwan Oh,[b,d] Mary C. Scott,[b,c,e], Armando Rodriguez-Campos [f, g],
Cynthia Huang,[f, h] Marie F. Millares,[f, h] Alexis Pace,[f] Lu Ma,[j] Steven Ehrlich,[j] Jianming Bai,[j]
Yimei Zhu, [h, k] Esther S. Takeuchi,[f, g, h, i] Amy C. Marschilok,[f, g, h, i] Shan Yan,[f, i] Kenneth J.
Takeuchi,[f, g, h, i]* and Marca M. Doeff[a]*

a) Energy Storage and Distributed Resources Division, Lawrence Berkeley National Laboratory, Berkeley CA, 94720 USA
b) The Molecular Foundry, Lawrence Berkeley National Laboratory, Berkeley, CA, 94720, USA
c) Department of Materials Science and Engineering, University of California Berkeley, Berkeley, CA, 94720, USA
d) Department of Energy Engineering, Korea Institute of Energy Technology (KENTECH), Naju, 58330, Jeonnam, Republic of Korea
e) Materials Sciences Division, Lawrence Berkeley National Laboratory, Berkeley, CA, 94720, USA
f) Institute of: Sustainability, Environment and Energy, Stony Brook University, Stony Brook, NY, 11794 USA
g) Department of Chemistry, Stony Brook University, Stonybrook, NY, 11794 USA
h) Department of Materials Science and Chemical Engineering, Stony Brook University, Stonybrook, NY, 11794 USA
i) Interdisciplinary Science Department, Brookhaven National Laboratory, Upton, NY, 11973 USA
j) National Synchrotron Light Source II (NSLS II), Brookhaven National Laboratory, Upton, NY, 11973 USA
k) Department of Condensed Matter Physics and Materials Science, Brookhaven National Laboratory, Upton, NY 11973, United States

*corresponding authors: (K.J.T.) kenneth.takeuchi.1@stonybrook.edu, (M.M.D.)
mmdoeff@lbl.gov

Keywords: Lithium-ion battery, anode, conversion electrode, spinel, compositionally complex materials

Abstract

Four different compositionally complex multi-component M_3O_4 spinels containing 5-8 distinct metals were prepared by a rapid combustion synthesis method or solvothermal synthesis. High resolution synchrotron X-ray diffraction patterns show that the materials consist primarily of spinel phases with small amounts of rock salt impurities, and, in several samples, a minor amount of contracted spinel phase. Materials were investigated as conversion anodes in lithium half-cells and delivered significantly higher capacities than two-component $MgFe_2O_4$ made by combustion synthesis. X-ray Absorption Near-Edge Spectroscopy (XANES) was used to estimate the oxidation states of the metals in the pristine, lithiated (discharged) and delithiated (charged) materials to better understand the redox processes in half cells that led to the improvement. Co, Ni, and Zn are reduced to low oxidation states during lithiation (cell discharge) but are only partially oxidized. The presence of a conductive metallic network that forms after lithiation is thought to account for the improved electrochemical characteristics. Interestingly, in most of the samples, iron is not fully reduced during initial lithiation unlike what happens with a set of related high entropy spinel ferrites studied previously. The improved electrochemical properties of these materials illustrates both the advantages of complexity and the difficulties in predicting their behavior.

Introduction

Metal oxide conversion anodes have been the subject of intense study for several decades.[1] During the initial lithiation in electrochemical cells, the metals are reduced and Li_2O is formed (equation 1).

$$(1) \qquad M_xO_y + 2yLi^+ \rightarrow xM + yLi_2O$$

This reaction is fully or partially reversible in Li-ion cells, often resulting in very high theoretical capacities. However, the electrodes suffer from poor rate capability and round-trip efficiencies (RTEs), hindering their adoption as anodes for Li-ion batteries. Strategies such as nano-structuring, incorporation of conductive additives like carbon nanotubes or reduced graphene oxide, and novel electrode designs have been used with some success to overcome these drawbacks,[2] although they often incur substantial energy density penalties. Since the initial report by Rost et al.[3] describing entropy-stabilized metal oxides, there has been increased interest in the role that configurational entropy plays in determining the physical and electrochemical properties of oxide materials. This concept has recently been applied to metal oxide conversion anodes.[4-7] We recently reported on a series of spinel ferrite conversion anodes containing 5-6 different metals[8] similar to those described in reference 9. The multi-component materials, which were not nanostructured, showed markedly better performance in lithium half-cells compared to a two-component spinel ferrite ($MgFe_2O_4$) prepared by the same synthesis method (SCS or solution combustion synthesis). A comprehensive XANES study showed that many of the metals in the multi-component spinel ferrites were reduced to the elemental state upon initial discharge (lithiation) but were not re-oxidized, providing an electrically conductive network that aids in charge transfer. Furthermore, in contrast to Fe_3O_4,[10] $MgFe_2O_4$, and $ZnFe_2O_4$[11] where Fe returns to the +2 oxidation state upon cell recharge, Fe is re-oxidized to an average oxidation state of about +2.6 in the more complex materials. The spinel ferrites in our previous study were designed to have multiple elements on tetrahedral sites, with the caveat that site-mixing cannot be ruled out in such complex materials (indeed EXAFS studies indicated that site-mixing did occur). For the present study, we synthesized four different M_3O_4 spinels containing equimolar amounts of 5-8 metals, without regarding their site occupancies. We refer to these materials as compositionally complex spinel oxides or CCSOs herein. As with the spinel ferrites, their electrochemical properties appear to be vastly superior to that of $MgFe_2O_4$ synthesized the same way. Here we describe their synthesis, characterization and electrochemical properties.

Experimental Methods

Solution Combustion Synthesis for the Preparation of Compositionally Complex Oxides. For the synthesis of multi-component CCSOs (nCCSO where n=5,6,7 or 8), a solution combustion synthesis (SCS)[12] was conducted using the following chemicals without further purification: metal nitrates, $Mn(NO_3)_2·4H_2O$, $Fe(NO_3)_3·9H_2O$, $Co(NO_3)_2·6H_2O$, $Ni(NO_3)_2·6H_2O$, $Zn(NO_3)_2·6H_2O$, $Mg(NO_3)_2·4H_2O$, $Al(NO_3)_3·9H_2O$, and titanium butoxide ($Ti(C_4H_9O)_4$). Initially, equiatomic ratios of the chemicals were dissolved in distilled water with continuous magnetic stirring for 1 h. For the Ti-precursor, it was dissolved in ethylene glycol and then mixed with the solution of dissolved metal nitrates. Subsequently, glycine as a fuel was added to the solution with a glycine-to-nitrate ratio of 0.56, and the mixture was stirred for an additional 30 min. The homogeneous solution was transferred to a beaker and placed on a hot plate. The solution was gradually heated, reaching a temperature of 300 °C, causing the water to evaporate and forming a viscous gel. Afterward, the gel combusted with self-ignition within tens of seconds, resulting in an ash-like combusted powder. This powder was ground into fine particles using a mortar. For comparison, the 2-component low-entropy oxide (2LEO, $MgFe_2O_4$) was prepared in the same manner. The materials made with 5-8 components are designated 5CCSO (Mn, Fe, Co, Ni, and Zn), 6CCSO (Mn, Fe, Co, Ni, Zn, and Mg), 7CCSO (Mn, Fe, Co, Ni, Zn, Mg, and Al), and 8CCSO (Mn, Fe, Co, Ni, Zn, Mg, Al, and Ti) hereafter, corresponding to the nominal compositions of $(Mn_{1/5}Fe_{1/5}Co_{1/5}Ni_{1/5}Zn_{1/5})_3O_4$, $(Mn_{1/6}Fe_{1/6}Co_{1/6}Ni_{1/6}Zn_{1/6}Mg_{1/6})_3O_4$, $(Mn_{1/7}Fe_{1/7}Co_{1/7}Ni_{1/7}Zn_{1/7}Mg_{1/7}Al_{1/7})_3O_4$, and $(Mn_{1/8}Fe_{1/8}Co_{1/8}Ni_{1/8}Zn_{1/8}Mg_{1/8}Al_{1/8}Ti_{1/8})_3O_4$, respectively.

Solvothermal Synthesis for the Preparation of Compositionally Complex Oxides. For the synthesis of the 5- and 8-component CCSOs, the following chemicals were used without further purification: $Mn(NO_3)_2{\cdot}4H_2O$, $Fe(NO_3)_3{\cdot}9H_2O$, $Co(NO_3)_2{\cdot}6H_2O$, $Ni(NO_3)_2{\cdot}6H_2O$, $Zn(NO_3)_2{\cdot}6H_2O$ (for the 5-component material) and $Mg(NO_3)_2{\cdot}4H_2O$, $Al(NO_3)_3{\cdot}9H_2O$, and titanium butoxide ($Ti(C_4H_9O)_4$) (for the 8-component material). Equiatomic ratios of the chemicals were dissolved in glycerol and iso-propanol to obtain 35 mL of the precursor with a total metal ion concentration of 0.04 M (0.005 M for each individual metal ion). The precursor solutions were then transferred to 45 mL PTFE-lined steel autoclaves, sealed, and placed in ovens at 180 °C. After 10 h, the autoclaves were removed from the ovens and allowed to cool in ambient air. The resulting products were washed several times with anhydrous ethanol and distilled water, then dried to obtain the powder. The obtained powders were further calcined at 700 °C for 6 h with a heating rate of 10 °C/min. These materials are designated 5CCSO-S and 8CCSO-S hereafter.

Structural and Morphological Characterization

The structures and phases of the samples were first characterized by laboratory X-ray diffraction (XRD, Bruker D2 Phaser). Synchrotron XRD measurements of as-synthesized products were conducted at the 28-ID-2 (XPD) beamline at National Synchrotron Light Source II (NSLS-II). The X-ray wavelength was calibrated to 0.185736Å and the detector was a 16-inch silicon panel equipped with a CsI scintillator. The Rietveld refinements of synchrotron XRD were performed with the GSAS-II software package.[13]

The crystal structure was visualized using VESTA software. The morphology of the samples was analyzed using a scanning electron microscopy (SEM, Zeiss Gemini Ultra-55, JEOL-6500F). The structure, morphology, and elemental distribution of the samples were observed using a transmission electron microscope (ThemIS, Thermofisher) equipped with an energy-dispersive X-ray spectrometry (EDS, Bruker Super X) analyzer. High Angle Annular Dark Field Scanning Transmission Electron Microscopy (STEM-HAADF) and additional EDS data was acquired using a FEI Talos operated at 200 kV equipped with a Super-X EDS system

The electrochemical mechanisms of 5CCSO, 6CCSO, 7CCSO, 8CCSO and 8CCSO-S were studied using *ex situ* X-ray absorption spectroscopy (XAS) at the QAS beamline (7-BM) in the National Synchrotron Light Source II at Brookhaven National Laboratory. Spectra were acquired at room temperature for Mn, Fe, Co, Ni, Zn and Ti K-edges. XANES analysis involved merging and processing spectra with Athena. The AUTOBK algorithm in Athena was used to reduce background contributions below R_{bkg} = 1.0 Å. Valence determination for Fe, Co, Ni and Ti utilized linear combination fitting (LCF) analysis with Athena from the Demeter package.[14] The selected energy range included -20 eV below to 30 eV above the edge energy for the least squares fitting of normalized μ(E) spectra. The edge energy is equal to the energy corresponding to a μ-value of 0.5 of the normalized spectra. The following standards were used for the LCF: Fe_2O_3, FeO and Fe_3O_4 for Fe, Co foil, CoO and $LiCoO_2$ for Co, Ni foil, NiO and $LiNiO_2$ for Ni, and TiO_2 and Ti_2O_3 for Ti, repectively. The oxidation state of zinc (Zn) is determined using the half-height method[15], which involves finding the edge energy value corresponding to a μ-value of 0.5 in the normalized spectra. This method is applied to zinc foil, $ZnCl_2$ and ZnO standards to establish calibration curves relating edge energy to the oxidation state of zinc. The oxidation state of Mn was evaluated through the integral method[15], applying calibration curves established with MnO, Mn_3O_4, Mn_2O_3, and MnO_2 standards.

Extended X-ray absorption fine structure (EXAFS) spectra fitting was performed using Artemis, with structural models generated by FEFF6. A Fe_3O_4 structural model with an $Fd\bar{3}m$ space group was employed and kept constant throughout the fitting of each K-edge. For the different edge energies , the core metal has been replaced, yet kept with the same space group and structure. For Co, Fe, Mn, and Ni across all samples, the fitting was conducted within a k-range of 3–11 $Å^{-1}$ using a Hanning window (dk = 1) in k, with k^2 and k^3 k-weights applied simultaneously, and an R-range of 1.0–3.5 Å. For Zn, a k-range of 2.5–12 $Å^{-1}$ was applied with the same Hanning window and k-weighting scheme, alongside an R-range of 1.0–3.5 Å. The S_0^2 parameters were determined based on reference materials and applied to all fits to account for the ratio of atoms located at tetrahedral and octahedral sites in the pristine CCSOs samples. [16-24] Furthermore, an impurity phase with a rocksalt structure ($Fm\bar{3}m$) was incorporated into the EXAFS fitting, informed by XRD refinement results using GSAS II, to provide a more accurate representation of atomic distributions.

The elemental composition for as synthesized CCSO samples was determined using inductively coupled plasma – optical emission spectroscopy (ICP-OES) using a ThermoScientific iCap 6300.

Electrode Fabrication. Composite electrodes were made by dissolving sodium carboxymethyl cellulose (CMC, Sigma-Aldrich) binder in distilled water, followed by the addition of the active material and conductive carbon (Denka). The slurry, consisting of the active material, binder, and conductive carbon in a weight ratio of 7:1:2, was then cast onto a Cu foil. Following casting, the electrode was dried overnight in a vacuum oven at 100 °C. The average loading level of the active material on the electrode was maintained at approximately 1.0–1.2 mg cm^{-1}.

*Electrochemical Measurements***.** For electrochemical performance evaluation, a 2032-type coin cell was assembled, utilizing a Li metal chip (MTI Corp.) as the counter/reference electrode, 1.0M $LiPF_6$ in a 1:1 (v/v) mixture of ethylene carbonate and diethyl carbonate as the electrolyte (SoulBrain, Co., Ltd), and Celgard 2400 (Celgard, LLC) as the separator. The cell assembly was carried out inside an Ar-filled glove box to maintain an inert atmosphere. CV measurements were conducted using a Biologic VSP multichannel potentiostat for two cycles with a scan rate of 0.2 mV/s. Galvanostatic battery cycling and rate capability tests were performed on a Biologic VSP multichannel potentiostat. The galvanostatic cycling for the CCSO half cells used for ex situ XAS was conducted using a MACCOR multichannel testing system. The test was conducted at 200 mA/g in a voltage window of 3.0-0.05V vs. Li/Li^+ at 30 °C.

Results and Discussion

Synthesis and Characterization of Compositionally Complex Oxides

In **Figure 1b**, a spinel structure is illustrated showing three different sites delineated by color. The red-colored spheres represent the anion (O^{2-}) site within the structure. Cations can occupy two distinct sites: one octahedral (in cyan) and the other tetrahedral (in dark blue). Site preferences depend on the oxidation state and type of cation for simple spinel oxide systems (e.g., those with two types of metal cations) and have been well-documented in the literature. However, high-entropy oxide systems are considerably more complex and cations can follow specific rules based on their valence states or occupy sites randomly.[9] Consequently, defining what high configurational entropy is for spinels is more complex than for the rock-salt structure due to these two different cation sites. Details of the atomic occupancies may influence the structural and electrochemical properties in unusual ways. Drawing from initial attempts to define high-entropy materials, it is established that these materials should have a configurational entropy value equal to or greater than 1.5R, where R is the ideal gas constant.[16] This value is maximized when the elements are present in equiatomic proportions. Achieving a configurational entropy value higher than 1.5R requires the presence of five different cations, assuming no anionic substitutions or vacancies on oxygen sites and only one sublattice for cations. We initially aimed to design high entropy spinel oxides, preparing compositions with 5, 6, 7, and 8 equimolar components. These would correspond to configurational entropy values of 1.61R, 1.79R, 1.95R, and 2.08R (the constant is obtained by lnN, where N is the number of components), assuming equal distribution of cations over the two types of sites, no short range order, no vacancies or substitutions in the anion lattice, and only one oxidation state for each metal. It is difficult to determine the site occupancies of each metal in multi-component spinel structures without extensive characterization beyond XRD, however. Furthermore, a recent paper[17] has pointed out challenges in calculating configurational entropy for complex crystal structures and questions whether the standard of 1.5R is relevant to ceramic materials. This value is derived from the entropy of fusion in metals, and results in an increased melting temperature, stabilizing the solid form. 1.5R also matches the internal energy of an ideal monatomic gas. The authors of the paper cited above have proposed a new configurational entropy metric for complex oxides, which takes in account situations where there are several sublattices. There are a few different ways to achieve high entropy for these; e.g., multiple elements on one sublattice, or several on multiple sublattices. By this logic, five distinct metals distributed equally over the tetrahedral and octahedral sites of a spinel or located on just one site results in only low-medium entropy oxide materials. Note, however, that the possibility of multiple oxidation states for transition metals can increase the number of components (e.g, Fe^{2+} and Fe^{3+} count as two different species). Thus, it is difficult to assess the configurational entropies of the subject materials based simply on their nominal compositions

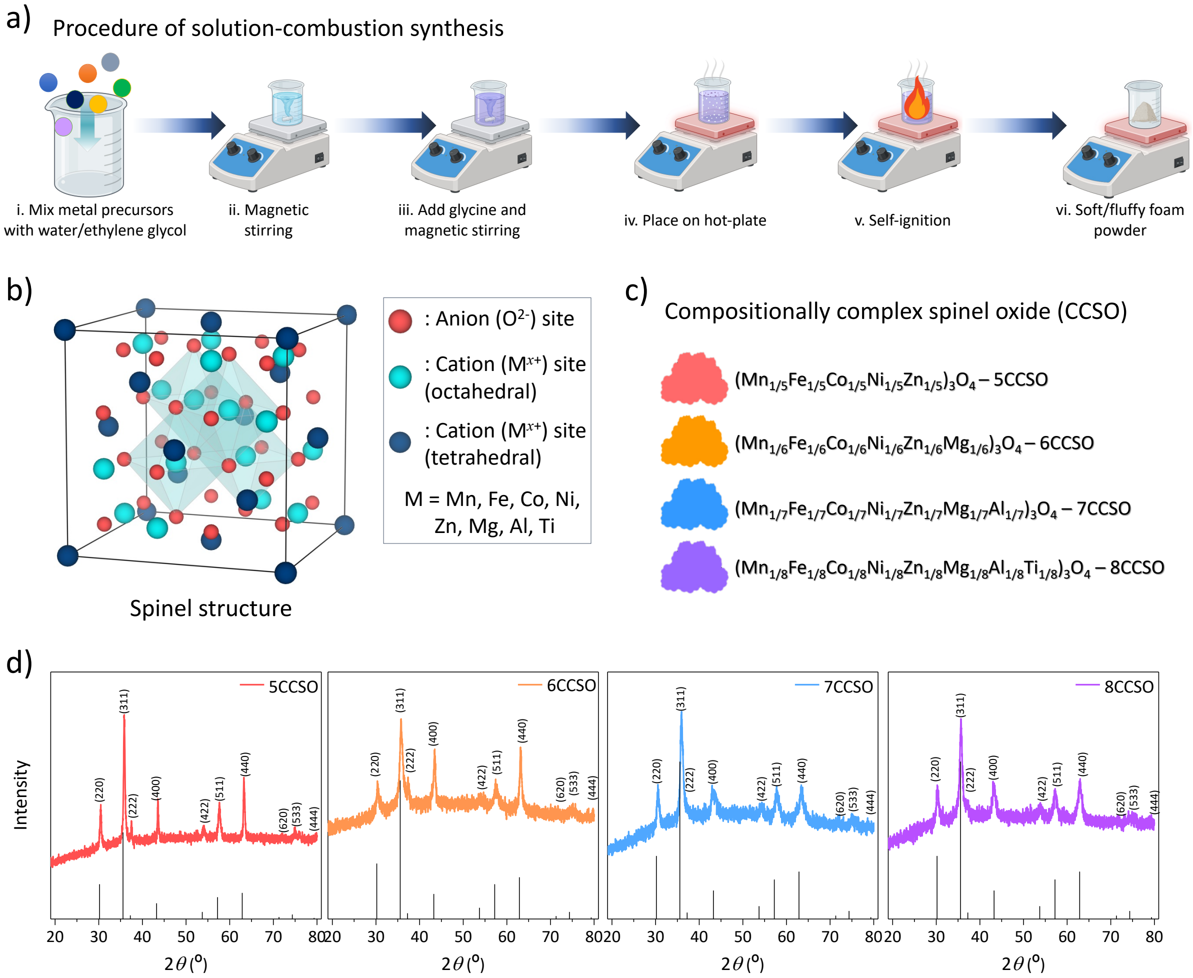

Figure 1. (a) Schematic showing solution combustion synthesis process used to make the listed CCSO spinels, reproduced from reference 8. Copyright 2024 American Chemical Society. (b) spinel structure. (c) compositions of materials, and (d) laboratory XRD patterns of the CCSOs made by combustion synthesis.

The multi-component oxides were prepared through solution-combustion synthesis (SCS) using metal precursors (Figure 1a) with the desired composition (Figure 1c). This method offers rapid synthesis and high yields. Four types of CCSOs were designed using the SCS approach (Figure 1c), denoted as 5CCSO, 6CCSO, 7CCSO, and 8CCSO, corresponding to the nominal compositions of $(Mn_{1/5}Fe_{1/5}Co_{1/5}Ni_{1/5}Zn_{1/5})_3O_4$, $(Mn_{1/6}Fe_{1/6}Co_{1/6}Ni_{1/6}Zn_{1/6}Mg_{1/6})_3O_4$, $(Mn_{1/7}Fe_{1/7}Co_{1/7}Ni_{1/7}Zn_{1/7}Mg_{1/7}Al_{1/7})_3O_4$, and $(Mn_{1/8}Fe_{1/8}Co_{1/8}Ni_{1/8}Zn_{1/8}Mg_{1/8}Al_{1/8}Ti_{1/8})_3O_4$, respectively. In addition, a two component spinel $MgFe_2O_4$ (2LEO) was prepared by the same procedure. CCSO materials containing 5 or 8 distinct metals were also prepared by a solvothermal synthesis procedure, and these will be discussed later. Figure 1d presents the laboratory XRD patterns of the SCS synthesized 5, 6, 7, and 8CCSOs. All XRD patterns of synthesized CCSOs closely matched the reference spinel structure of $MgFe_2O_4$ (JCPDS #72–1232). The peaks in the XRD patterns exhibited increased broadening as the number of components went up. The degree of peak broadening is most evident in 8CCSO but exhibited to a lesser degree in all the CCSOs. This is in contrast to a related set of high entropy spinel ferrites we reported on recently, which appear to be highly crystalline, judging from the narrowness of the reflections.[8] While compositional disorder resulting in an array of lattice spacings may be the cause of the peak broadening, it is significant that the spinel ferrites did not exhibit this feature and suggests that more careful structural characterization is needed.

For this reason, synchrotron XRD patterns were collected for all the materials (Figure 2) including 2LEO (Figure S1a). While the pattern of 2LEO matched that of $MgFe_2O_4$, those of the CCSOs are more complex than the lab XRD patterns indicate. The strongest peaks in the synchrotron patterns could be indexed to a major cubic spinel phase belonging to the $Fd\bar{3}m$ space group (COD ID: 9003582), but in two of them (5CCSO and 7CCSO), there are reflections belonging to another $Fd\bar{3}m$ spinel phase with a smaller lattice parameter. In addition, for all of the CCSOs, there is also a minority rocksalt phase that can be indexed to the $Fm\bar{3}m$ space group (COD ID: 9006073). The resulting structural parameters calculated from Rietveld refinement are given in Tables S1 and S2. The unit cell parameters of the main spinel phase vary among the CCSOs, with 7CCSO having the smallest lattice (8.3015 (4) Å) while 8CCSO has the largest (8.3470 (3) Å). This indicates that the compositions of the main spinel phases are not all the same. It is also notable that the amount of microstrain increased with number of components for these phases up to 7CCSO, suggesting that more elements may have been incorporated into them.

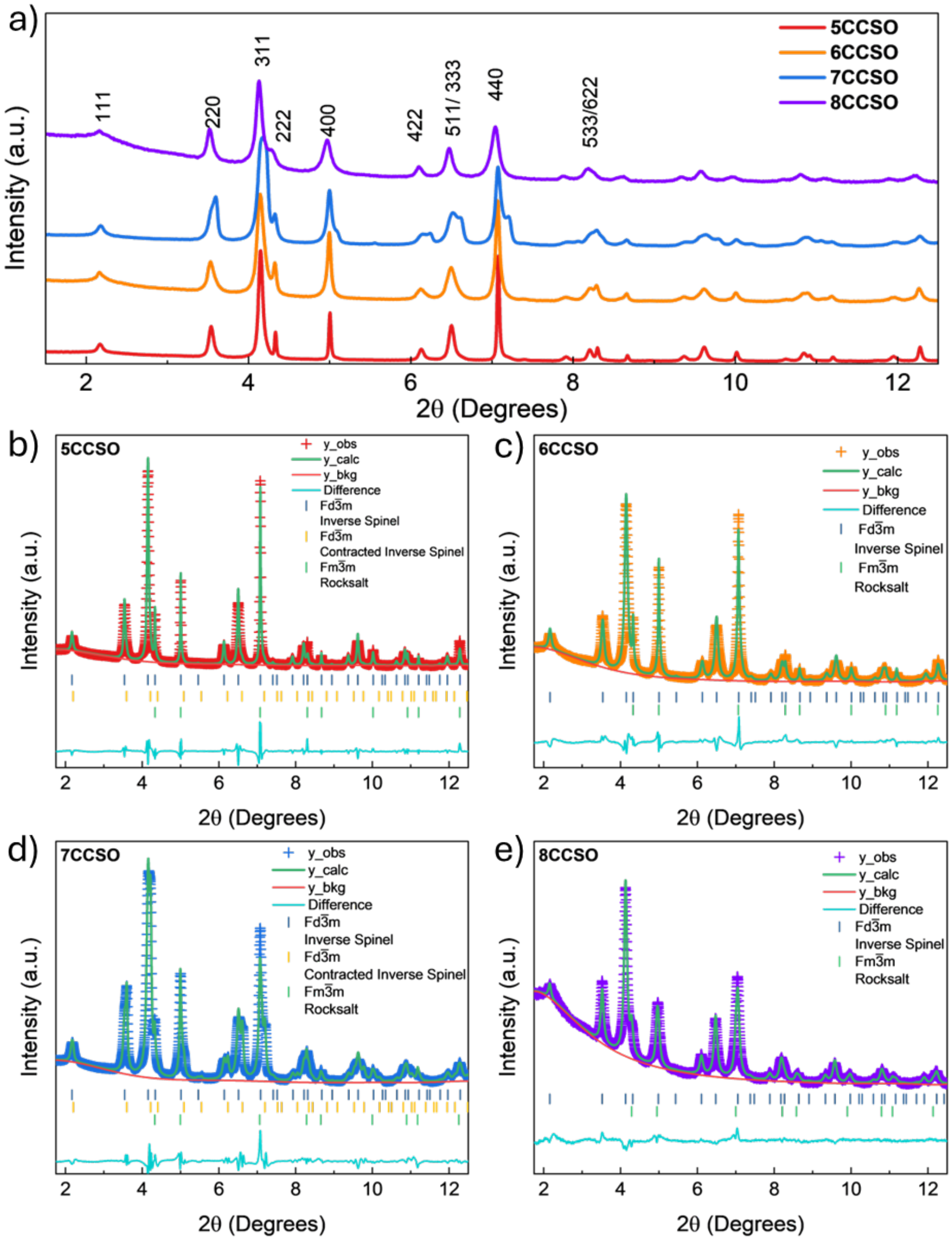

Figure 2. (a) Synchrotron XRD patterns of 5CCSO (in red), 6CCSO (in orange) , 7CCSO (in blue), and 8CCSO (in purple). (b-e) Rietveld refinement plots of 5CCSO (b), 6CCSO (c), 7CCSO (d), and 8CCSO (e).

Table 1. Phase fractions of CCSOs determined from Rietveld refinement.

Phases	Main spinel ($Fd\bar{3}m$)	Contracted spinel ($Fd\bar{3}m$)	Rocksalt phase ($Fm\bar{3}m$)	R_{wp}(%)
5CCSO	88%	8%	4%	9.78
6CCSO	91%	-	9%	6.70
7CCSO	64%	30%	6%	6.75
8CCSO	89%	-	11%	3.01
2LEO	73%		27%	5.45

The presence of multiple phases in these samples (Table 1) further complicates their description. It is not possible to assess from XRD analysis alone what elements are present in each phase, how much of each element is present in each phase, or what sites they occupy in the spinel phases. While it appears that the compositions of the main spinel phases did vary as more elements were added, it is not clear whether the CCSOs in this study fit the strict definition of high entropy oxides as discussed above. For this reason, we refer to them here as compositionally complex or variable entropy materials.

Additional structural insights were obtained from X-ray absorption near edge spectra (XANES) measurements of the 5CCSO, 6CCSO, 7CCSO and 8CCSO pristine samples collected at Mn, Fe, Co, Ni, Zn, and Ti K-edges for the valence determination of the metal centers (Figure 3). Examining Mn K-edge XANES in Figure 3a, 8CCSO aligns closely with the reference Mn_2O_3, suggesting an oxidation state of +3, while the spectra of 5CCSO, 6CCSO, and 7CCSO are closer to MnO_2, indicating an oxidation state around +4. Additionally, the absorption edge intensity of the pristine 8CCSO sample is notably lower than that of 5CCSO, 6CCSO, and 7CCSO spectra. In Figure 3b, the Fe XANES spectra exhibit a similar energy edge, differing in absorption intensity around 7133 eV. Specifically, the spectra of 5CCSO and 8CCSO display lower intensity compared to 6CCSO and 7CCSO. The observed edge positions suggest an oxidation state around Fe^{3+}. The XANES at the Fe K-edge of 2LEO ($MgFe_2O_4$) also suggests Fe^{3+}, as shown in Figure S1. Moving to the Co K-edge (**Figure 3c**), a noticeable difference in edge position is evident, with 8CCSO displaying a much lower energy edge, approaching the energy of C_OO with an oxidation state of +2. In contrast, the spectra of 5CCSO, 6CCSO, and 7CCSO fall between the spectra of CoO and $LiCoO_2$, indicating an oxidation state around 2.5. For the Ni K-edge (**Figure 3d**), the spectrum of

5CCSO - 8CCSO presents a similar energy edge but 8CCSO presents a lower intensity compared to the spectra of the other three samples. Linear combination fitting indicates an Ni oxidation state of around 2 for the pristine samples. In the Zn-edge (**Figure 3e**), all four samples exhibit similar absorption spectra, with the energy edge appearing at the same position corresponding to an oxidation state of +2, based on the reference of $ZnCl_2$. Considering the Ti element in 8CCSO (**Figure 3f**), the Ti K-edge positions suggest an oxidation state between Ti^{3+} and Ti^{4+}, as compared to the energy levels of the Ti_2O_3 and TiO_2 reference materials. Linear combination fitting indicates a pristine electrode Ti oxidation state of approximately 3.90. Average oxidation states for the different metals in the CCSO samples and their oxygen contents, calculated using charge balance assumptions are summarized in Table 2.

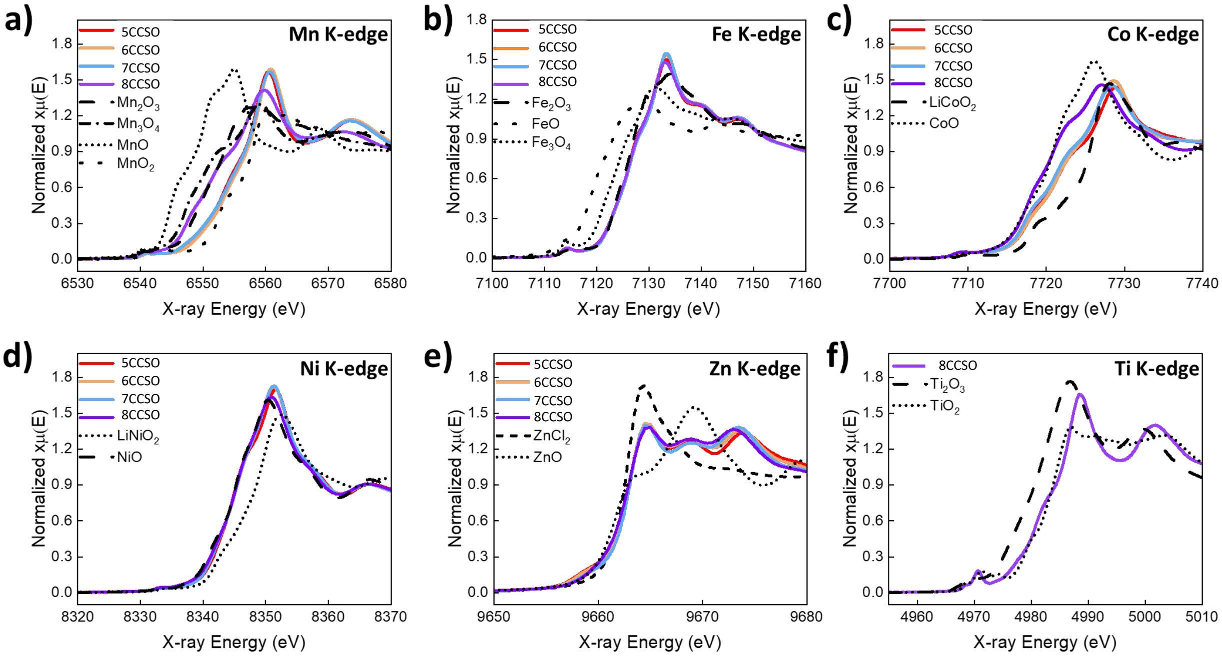

Figure 3. XANES spectra of nCCSO powder samples and standards at (a) Mn K-edge, (b) Fe K-edge, (c)Co K-edge, (d) Ni K-edge, (e) Zn K-edge and (f) Ti K-edge.

The elemental composition was confirmed by inductively coupled plasma optical emission spectroscopy (ICP-OES). Coupled with oxidation states determined by XANES, the actual compositions of the CCSO powders are given in Table 2, and are reasonably close to the nominal ones.

Table 2. Average metal oxidation states and formulas of CCSOs.

Sample	Oxidation states						Composition
	Mn	Fe	Co	Ni	Zn	Ti	
5CCSO	3.7	3.0	2.6	2.2	2.0	/	$(Mn_{0.20}Fe_{0.20}Co_{0.19}Ni_{0.21}Zn_{0.18})_3O_{3.98}$
6CCSO	3.8	3.0	2.6	2.2	2.0	/	$(Mn_{0.16}Fe_{0.17}Co_{0.15}Ni_{0.17}Zn_{0.16}Mg_{0.17})_3O_{3.81}$
7CCSO	3.7	3.0	2.6	2.2	2.0	/	$(Mn_{0.15}Fe_{0.14}Co_{0.14}Ni_{0.16}Zn_{0.12}Mg_{0.15}Al_{0.06})_3O_{3.62}$
8CCSO	3.1	3.0	2.2	2.1	2.0	3.9	$(Mn_{0.12}Fe_{0.13}Co_{0.12}Ni_{0.13}Zn_{0.12}Mg_{0.13}Al_{0.18}Ti_{0.11})_3O_{4.15}$

There are some differences between the CCSO materials and the spinel ferrites that were the subject of our previous investigation.[8] While both sets of materials contain Fe in the trivalent state, and Co and Ni are close to +2 in all the pristine samples, the oxidation states of Mn in the CCSO series is higher than those of the Mn-containing spinel ferrites. There, the average oxidation states of Mn is between +2 and +3, whereas they are above +3 in the CCSOs, and close to +4 for most of the samples. This is a consequence of the decreased amount of Fe^{3+} and the increased content of cations in the +2 oxidation state, which requires a higher oxidation state for Mn for charge compensation. Notably, Mn in 8CCSO is at a lower oxidation state, because of the presence of Ti^{4+}.

EXAFS analysis was used to understand the distributions of probed metals between octahedral and tetrahedral sites in the spinel and in octahedral sites of rock salt phases in the CCSO materials made by SCS. These data are presented in Figure 4 and Table 3. Comprehensive fitting parameters and results are also provided in Tables S3-S6. While the spinel phases contain all of the metals that were investigated, the rocksalt phases contain only two or three, in particular some Co and Fe. Ni is missing from most of the rock salt phases, except for 6CCSO, and Zn is additionally present in the 5CCSO rock salt phase, and Mn in the 8CCSO. Ni appears to show a strong preference for octahedral sites over tetrahedral sites in the spinel phases. The rest of the metals are distributed randomly over both octahedral and tetrahedral sites. Most notably, Fe appears to be roughly equally distributed between the two types of sites, in most cases, similar to what was found in the spinel ferrites made by combustion synthesis.[8]

Figure 4 shows the Fourier transform (FT) of the R-space extended X-ray absorption fine structure (EXAFS) spectra of Co, Fe, Mn, Ni and Zn. To access the distribution of metal atoms in the crystal structure in pristine CCOS samples, the Extended X-ray Absorption Fine Structure (EXAFS) fitting was applied through the Artemis software. EXAFS fitting facilitated the determination of the interatomic distances between the core metal and its neighboring O or metal atoms, as well as the distribution percentage of tetrahedrally and octahedrally coordinated metal atoms, as depicted **Table 3** with detailed fitting parameters and comprehensive results.

The EXAFS spectra of Fe, Ni and Zn in samples 5CCOS-8CCOS display similar patterns.In Fe-edge spectra, a distinct peak is evident at approximately 1.5 Å and the second main peak shown at around 2.6 Å with a shoulder peak located at around 3.2 Å. The peak at 1.5 Å arises from the nearest neighboring oxygen atoms bonded to the core Fe atoms, while the peak at 2.6 Å originates from the nearest neighbor Fe atoms and second shell oxygen atoms. The shoulder peak is located at around 3.2 Å, which arises from Fe atoms in the tetrahedral environment. Based on the EXAFS fitting results, around half of the Fe atoms are located at octahedral sites in the spinel phase and approximately half are located at tetrahedral sites. The intensity of the second main and shoulder peak varies due to the ratios of octahedral and tetrahedral sites distribution.[10] These findings suggest the presence of Fe atoms not only in tetrahedral sites but also in octahedral sites.

The Ni-edge EXAFS spectra exhibit two primary peaks at approximately 1.6 Å and 2.5 Å, corresponding to the core Ni atom's interactions with its nearest neighboring oxygen atoms and Ni atoms, respectively. Due to the similarities between the EXAFS spectra of NiO and Ni_2O_3,[6] EXAFS fitting was employed to further clarify atomic positions. The fitting results indicate that all Ni atoms are located at octahedral sites within the spinel phase, rather than tetrahedral sites.

In the Zn-edge spectra, a prominent peak is observed at around 1.5 Å, which is attributed to the nearest neighboring oxygen atoms bonded to the core Zn atoms. Another significant peak, observed at approximately 3.0 Å, is attributed to Zn–Zn paths. The EXAFS fitting results indicate that approximately half of the Zn atoms occupy octahedral sites, while the remainder are positioned at tetrahedral sites.

The Fourier transform (FT) of the R-space EXAFS spectra for Co reveals differences among the four samples, particularly in the 8CCOS sample. In samples 5CCOS to 7CCOS, two dominant peaks are observed at 1.5 Å and 2.5 Å, corresponding to the core atom to the nearest neighboring oxygen atoms and the nearest neighboring Co atoms, respectively. A shoulder peak around 3.0 Å indicates Co atoms located in tetrahedral environments. However, in the Co-edge EXAFS spectra of 8CCOS, only two peaks are evident at approximately 1.5 Å and 2.5 Å. The EXAFS fitting results further indicate that Co atoms are distributed between tetrahedral and octahedral sites in samples 5CCOS to 7CCOS, while in the 8CCOS sample, all Co atoms are exclusively located at octahedral sites within the spinel phase.[6] The presence of a shoulder peak suggests that, in some samples, Co atoms are distributed across both octahedral and tetrahedral sites.

The Fourier transform (FT) of the R-space EXAFS spectra for Mn from 5CCOS to 8CCOS exhibits variation across the samples. In samples 5CCOS to 7CCOS, two primary peaks are detected at around 1.5 Å and 2.5 Å, which correspond to the core Mn atom's nearest neighbor oxygen atoms and the Mn–Mn interactions at octahedral sites. In contrast, in the 8CCOS spectra, the first peak remains at approximately 1.5 Å, attributed to Mn–O coordination, while the second peak shifts slightly to 2.6 Å and becomes broader, potentially indicating the merging of two distinct peaks. Based on EXAFS fitting, approximately 70% of Mn atoms are located at octahedral sites in samples 5CCOS to 7CCOS, with the remaining 30% in tetrahedral sites. In sample 8CCOS, this distribution is reversed, with approximately 30% of Mn atoms occupying octahedral sites and 70% in tetrahedral sites.

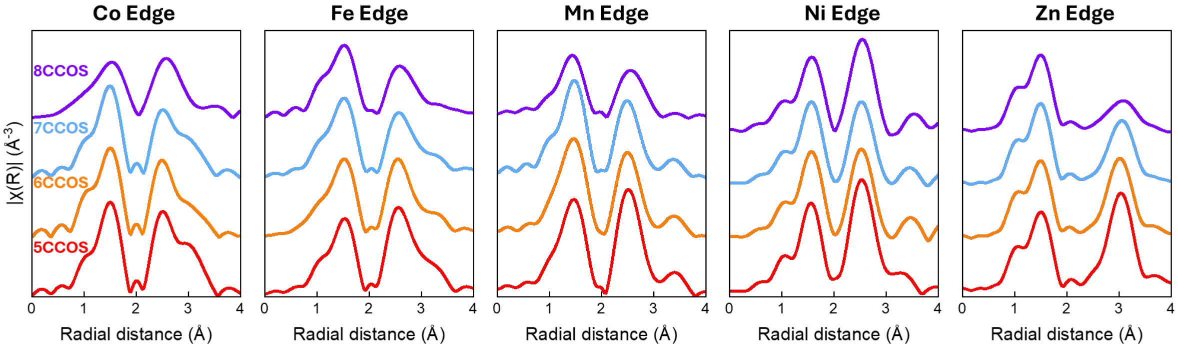

Figure 4. Extended X-ray absorption fine structure (EXAFS) spectra of 5CCSO, 6CCSO, 7CCSO, and 8CCSO at Co, Fe, Mn, Ni and Zn K-edges.

Table 3 : EXAFS fitting results, showing fractions of selected metals in compositionally complex oxide spinels

Sample		Spinel Phase Fd-3m		Rocksalt Fm-3m	R-factor
		Octahedral site	Tetrahedral site	Octahedral site	
5CCSO	Co	0.66	0.24	0.1	0.001
	Fe	0.47	0.44	0.09	0.001
	Mn	0.76	0.24	0	0.001
	Ni	1.00	0	0	0.006
	Zn	0.45	0.49	0.06	0.008
6CCSO	Co	0.58	0.31	0.11	0.004
	Fe	0.54	0.35	0.11	0.001
	Mn	0.69	0.31	0	0.004
	Ni	0.77	0	0.23	0.009
	Zn	0.49	0.51	0	0.010
7CCSO	Co	0.59	0.3	0.10	0.001
	Fe	0.49	0.35	0.16	0.001
	Mn	0.63	0.37	0	0.001
	Ni	1.00	0	0	0.008
	Zn	0.55	0.45	0	0.008
8CCSO	Co	0.75	0	0.25	0.005
	Fe	0.3	0.41	0.29	0.003
	Mn	0.22	0.66	0.12	0.006
	Ni	1.00	0	0	0.010
	Zn	0.62	0.38	0	0.008

The particle morphologies and elemental distributions in the CCSO powders were investigated using scanning electron microscopy (SEM) and transmission electron microscopy (TEM) with energy dispersive X-ray spectroscopy (EDS). SEM images of nCCSO materials synthesized with the SCS process reveal micrometer particles composed of sub-micrometer particles with nanometer pores (Figure S2). 2LEO made by the SCS process has a similar morphology (Figure S1b). These images show that the constituent particles were uniformly dispersed and agglomerated, forming a complete porous framework. This porous structure, developed during the exothermic combustion reaction, was a result of the substantial release of gas during the nucleation of the oxides, hindering crystal growth. The porous framework was consistently observed in all CCSO samples. However, in the case of 8CCSO samples, the microstructure appeared denser, and porosity was lower compared to the other samples (Figure

S1d). This difference may be attributable to the use of titanium butoxide as a precursor material, which may affect the reaction temperature and the amount of gas that is liberated during combustion.[18]

Figure S3 shows TEM analysis for the CCSOs. High-Resolution TEM (HR-TEM) images confirm the crystalline nature of all CCSO samples. Several crystals are randomly oriented with respect to one another and, in some cases, overlap. It was still possible to identify lattice planes, marked in the Figure. Additionally, the electron diffraction patterns of all CCSOs (inset in HR-TEM images) correspond to the crystal planes of the spinel structure. Furthermore, elemental mapping *via* high-angle annual dark-field scanning transmission electron microscopy (HAADF-STEM) combining EDS map images confirms the spatially uniform distributions of O, Mn, Co, Fe, Ni, and Zn (for 5CCSO); O, Mn, Co, Fe, Ni, Zn, and Mg (for 6CCSO); O, Mn, Co, Fe, Ni, Zn, Mg, and Al (for 7CCSO); and O, Mn, Co, Fe, Ni, Zn, Mg, Al, and Ti (for 8CCSO), respectively. Additional images from a different set of particles are shown in Figure S4. This shows that the component elements of each sample are well distributed within each particle with even proportions (typical particles are within 5% of equimolar compositions), with no notable surface or domain segregation.

Electrochemical Properties of CCSOs made by SCS

Cyclic voltammetry (CV) was conducted to study the redox reactions and structural transformations during the Li-insertion/extraction process. Figure 5a-d shows the CV curves recorded in the 0.01–3.0 V potential range at a scan rate of 0.2 mV s^{-1}, corresponding to rates of about C/17. In the first cathodic scan (discharge, lithiation), a single large peak appeared below 0.5V, with the exact position somewhat dependent on CCSO composition. As the number of metals increased, the position shifted to a lower value. This peak can be assigned to the reduction reactions of electrochemically active cations, along with the formation of Li_2O and irreversible changes in the crystal structure. Typically, the CVs of transition metal oxide spinel conversion anodes show multiple peaks on the first cycle corresponding to insertion of lithium followed by structural rearrangement and displacement reactions, as well as formation of a solid electrolyte interphase (SEI).[19] However, the first cycle CV curves for the CCSO-containing cells show only one cathodic peak, meaning that these processes overlap, and metals are reduced concurrently, rather than in a stepwise fashion. Upon re-oxidation (charge, delithiation), only one peak is observed, which can be ascribed to the re-oxidation process of the redox-active species, along with the decomposition of Li_2O. This process is chemically reversible.

The Li^+-storage performance of the CCSO electrodes was investigated in half cells with Li-metal anodes by recording galvanostatic charge-discharge (GCD) curves. Figure 5e-h displays the GCD curves of cells containing the CCSOs for the first three cycles at a current density of 200 mA g^{-1} (roughly C/13). During the initial discharge, there is an initial sloping portion followed by a single long plateau and another sloping region. The plateau voltages vary only slightly with CCSO composition, ranging from about 0.75V for 5CCSO to 0.6V for 8CCSO, and are similar to those found for a series of high entropy spinel ferrites that have been recently reported.[8] The initial discharge and charge capacities are given in Table S7, as well as theoretical values based on complete reduction of all metals to the elemental state (equation 2).

$$(2) \qquad M_3O_4 + 8Li^+ + 8e^- \rightarrow 3M + 4Li_2O$$

The theoretical capacities rise as the number of components in the CCSOs increase, because of partial replacement of heavier metal ions (Fe, Co, Ni, Mn) with lighter ones such as Mg, Al, and Ti. In practice, however, complete reduction of all the metal ions may not occur, and metals may not be reoxidized to their original state. Additional capacity may arise from alloying reactions and/or interfacial storage.[1] Lithium insertion into the acetylene black conductive additive may also contribute some capacity, although this is very small (see Figure S2 in reference 20). Most importantly, during the first discharge, irreversible reactions involving decomposition of electrolyte and other cell components lead to formation of a solid electrolyte interphase (SEI), occuring at potentials below 1V. This results in first discharge capacities higher than predicted. Initial Coulombic efficiencies (ICE, Table S7) were inversely proportional both to initial discharge capacities and the number of components in the CCSOs. After the first cycle, Coulombic efficiencies (CE) approach 100% for all of the CCSO-containing cells.

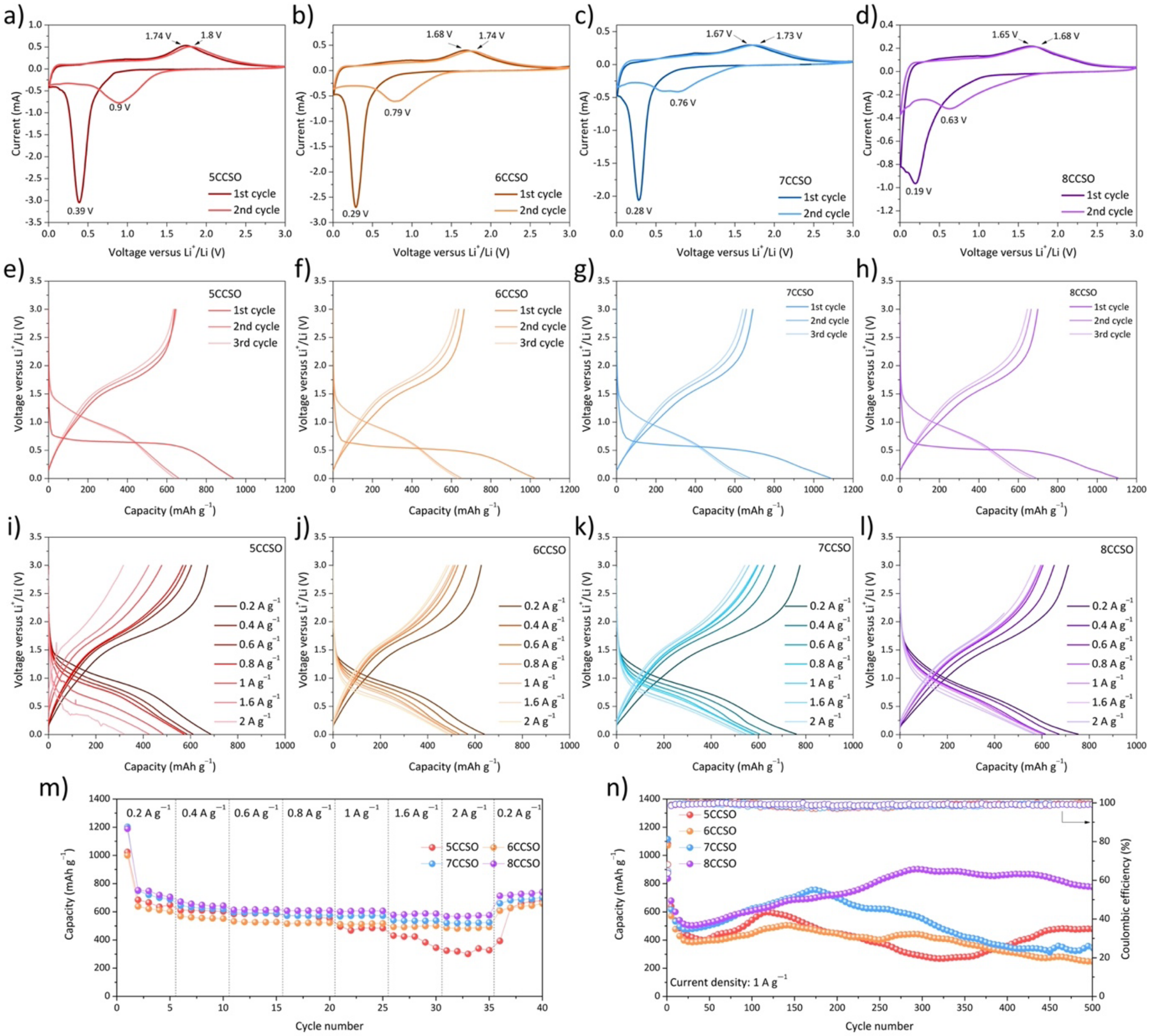

Figure 5.(a-d) CVs at 0.2 mV/sec, (e-h) galvanostatic discharge/charge curves at 0.2 Ag^{-1} , (i-l) rate capability tests, (m) capacity as a function of cycle number at various rates, and (n) capacity as a function of cycle number at 1Ag^{-1} for cells containing 5CCSO, 6CCSO, 7CCSO, and 8CCSO anodes, as indicated.

The rate capability of CCSOs in lithium half-cells was evaluated by varying the current density from 400 to 2000 mAg$^{–1}$, stepped in increments of 200 mAg^{-1} (Figure 5i-m). 8CCSO exhibits the highest capacities at every current measured, although differences are fairly small for all the CCSOs at current densities below 1Ag^{-1}. Above this rate, 5CCSO cells are significantly worse those containing 6, 7, and 8CCSOs. This strongly suggests significant advantages associated with increased complexity for these materials when used as conversion anodes. Strengthening this argument is the observation above that the 8CCSO material appears to be somewhat less porous than the CCSOs with fewer components, but it still performs better than the other CCSOs, ruling out morphological factors.

To further verify the entropic effect, 2LEO, $MgFe_2O_4$, was also prepared by combustion synthesis and evaluated under the same conditions as the CCSOs for comparison (Figure S1c and d). Interestingly, both the reversible capacities and ICEs of cells containing all the CCSOs are noticeably higher than those of 2LEO. The obtained capacities of cells containing 2LEO are much lower than its theoretical value, and the performance is markedly worse than that of nanostructured $MgFe_2O_4$.[21,11] Figure S5 compares capacities as a function of cycle number for the CCSOs and 2LEO at a current density of 200 mA g^{-1} and Figure 5n shows data for the CCSO cells using a current density of 1 Ag^{-1}. All the CCSO electrodes exhibit similar behavior initially regardless of rate; a decrease in capacity during the first few cycles, followed by a gradual rise to a maximum value. This is a commonly observed behavior for conversion anodes[22] and has been attributed to increased surface area and surface storage due to "electrochemical grinding", formation of electroactive interphases and other phenomena. The increase in capacity is also observed for the 2LEO cell, although capacities were still much lower than expected even after 150 cycles. The tendency for capacity to increase during cycling has been previously observed in conversion-based oxide anodes and has been attributed to increased porosity and surface storage and decomposition of electrolyte, among other factors.[22] For some of the CCSOs, it appears that capacities approaching the theoretical values according to equation 1 are reached during later cycles, although the phenomena described above complicate interpretation of the electrochemical data. Improving cycling stability may require the use of electrolyte additives and other strategies commonly used in lithium-ion batteries.

After reaching their maximum values, capacities decreased for the cells containing 5CCSO, 6CCSO, and 7CCSO at the higher rate, and for 5CCSO and 6CCSO at the lower one. 8CCSO shows the highest reversible capacity of 776 mAh g^{-1} after 500 cycles at 1Ag^{-1} and stable capacity retention during cycling. Hence, among the CCSOs, 8CCSO exhibits the best performance based on reversible capacity, rate capability, and long-term cycling stability.

Properties of CCSOs made by solvothermal synthesis

8CCSO was also synthesized by solvothermal synthesis and is denoted 8CCSO-S. The laboratory XRD patterns of 8CCSO-S matches well with a reference spinel structure (JCPDS #72–

1232, Figure 6), but, as with the XRD patterns of 8CCSO synthesized by the SCS method, the reflections are broad. The SEM images show nearly monodisperse 8CCSO-S particles with a sphere-like morphology, having a diameter of approximately ~1.5 µm (Figure 6b). Additionally, each element (metal cations and oxygen) is well-distributed, as confirmed by SEM/EDS results (Figure 6c).

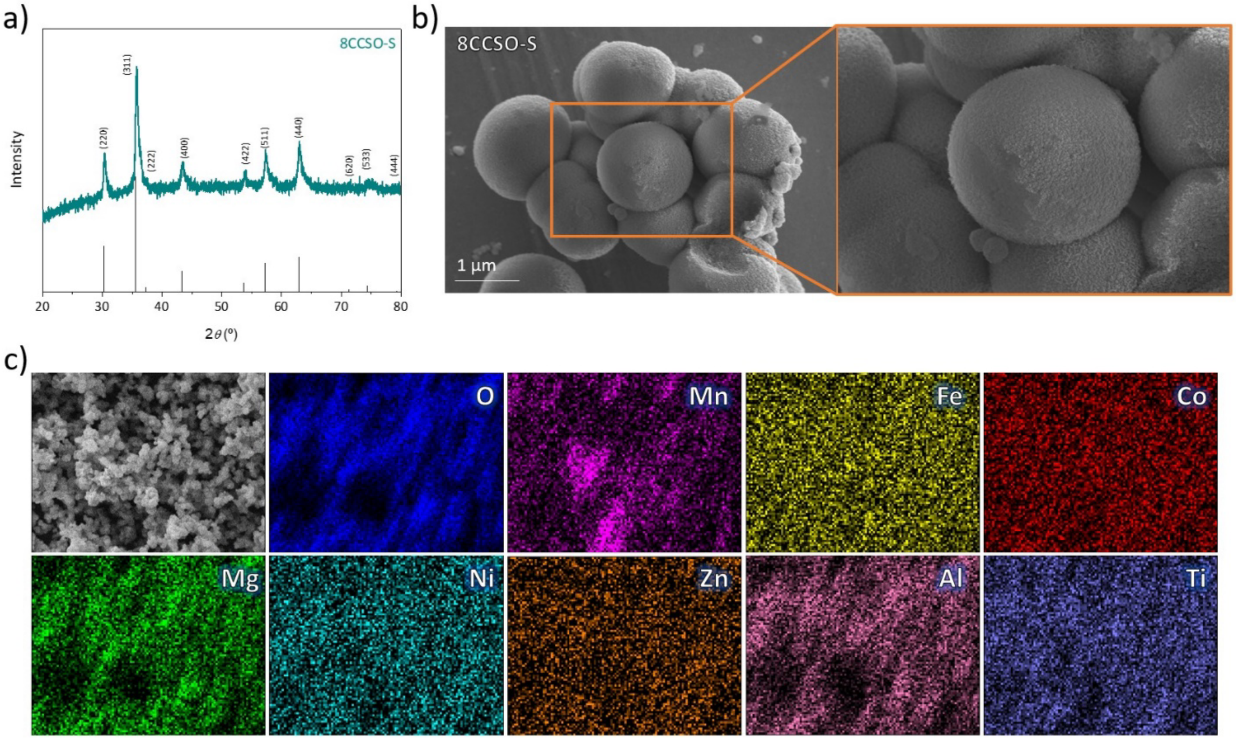

Figure 6. (a) Laboratory XRD pattern of 8CCSO-S made solvothermally, (b) high-magnification SEM images of 8CCSO-S particles, and (c) SEM-EDS results on 8CCSO-S showing homogeneity of metal distributions.

The synchrotron XRD pattern of 8CCSO-S is shown in Figure S6 and the refined parameters are detailed in Tables S1 and S2. 8CCSO-S is composed of 68% cubic spinel phase and 28% contracted spinel, as well as some rocksalt phase (4%). The lattice parameter of the main phase is slightly larger than that for 8CCSO and the crystallite size is also larger (Table S1). The microstrain is similar to that of 7CCSO and higher than that of 8CCSO. These observations all suggest that the distribution of metals in the main spinel phase in 8CCSO-S differs from that of the one in 8CCSO.

STEM-HAADF imaging was also carried out on this sample to understand the distributions of the metals (Figure S7 and Table S8). The 8CCSO-S sample demonstrates more complex segregation behavior than the samples made by SCS. The primary synthesis product are spheres with a metal composition described in Table S8 with some minor product observed, which has different stoichiometry. While the spheres contain all 8 component elements, they are not in an equimolar ratio. In addition to phase segregation, the spheres have a core-shell-shell structure, with segregation of Fe and Co (and slight Ni) to the outer surface (~0-50 nm from surface), enrichment of Al in a subsurface layer (from ~50-100 nm from surface), and depletion of Ti and Zn from the surface as seen in Figure S7b.

The K-edge XANES spectra oxidation states of the Mn, Fe, Co, Ni, Zn, and Ti metal centers of 8CCSO-S are similar to those of 8-CCSO with only slight variations (Figure 7**)**. The oxidation states of Mn and Co for 8CCSO-S are slightly higher than for 8CCSO, specifically, +3.43 v.s. +3.08 for Mn and +2.43 v.s. +2.19 for Co for 8CCSO-S and 8CCSO, respectively. The oxidation states of Fe, Ni, Zn, and Ti are similar for both 8CCSO and 8CCSO-S, respectively, +3.00, +2.15, +2.00, and +3.99. Coupling this information with ICP-OES results, the global composition of 8CCSO-S is $(Mn_{0.13}Fe_{0.13}Co_{0.12}Ni_{0.13}Zn_{0.13}Mg_{0.13}Al_{0.16}Ti_{0.13})_3O_{4.39}$.

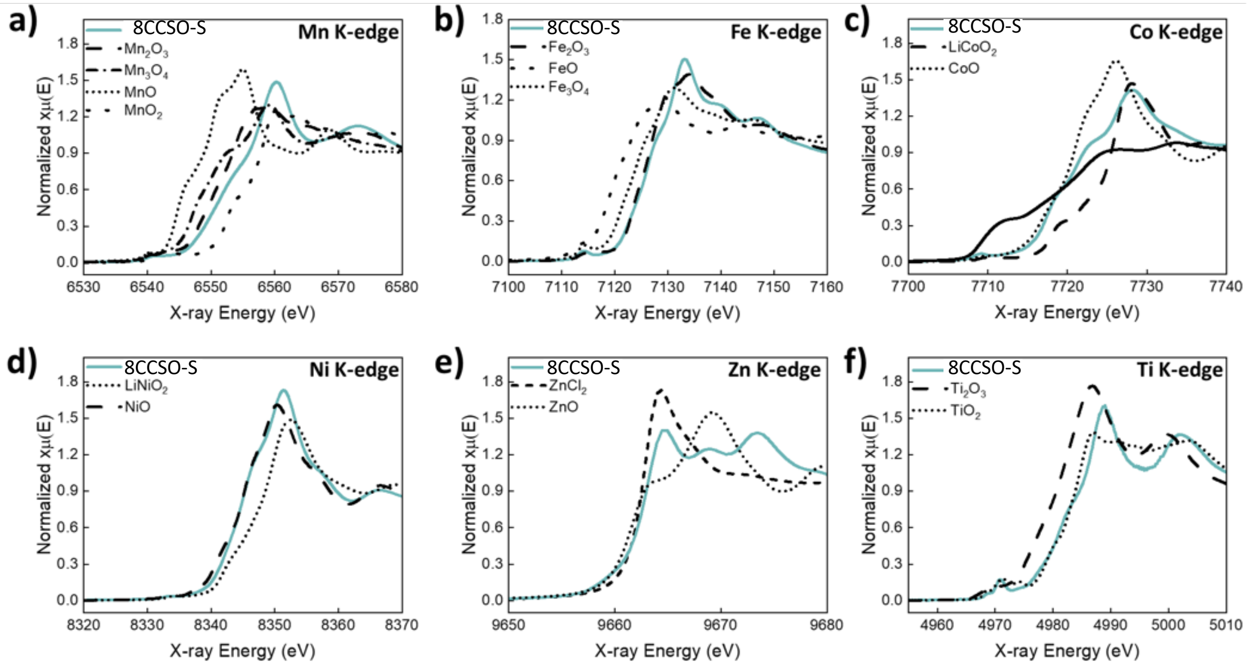

Figure 7. XANES spectra of 8CCSO-S and standards at (a) Mn K-edge, (b) Fe K-edge, (c)Co K-edge, (d) Ni K-edge, (e) Zn K-edge and (f) Ti K-edge.

As with the other CCSO materials, the EXAFS of 8CCSO-S (Figure S8) shows that there are more metals in the spinel phase(s) than in the rock salt phase (Table S9). Ni is also exclusively located in the octahedral site of the spinel, but distributions of the metals between octahedral and tetrahedral sites of the spinel are somewhat different from that of 8CCSO. For example, there is no Co located in the spinel tetrahedral sites of 8CCSO, but Co is distributed between the two different sites in 8CCSO-S. The variations in both phase and site distributions between 8CCSO and 8CCSO-S are not too surprising, given the different methods used to obtain the materials. Combustion synthesis is very rapid and can lead to kinetically stabilized products, while solvothermal synthesis is slower, allowing thermodynamic equilibration to take place.

An attempt was also made to synthesize 5CCSO-S solvothermally. The particles have "desert rose" morphologies (Figure S9 a and b**),** comprised of spherical particles about 1 um across, which are made up of smaller crystallites. This time, the laboratory XRD pattern (Figure S9c) quite clearly indicates that it is a phase mixture containing rock salt as well as two spinel phases.

Figure 8a shows the galvanostatic charge/discharge curves of the first three cycles of Li half-cells containing 8CCSO-S at a current density of 0.2 A g^{-1}. The shape of the initial discharge curve is different from that of 8CCSO made by SCS, showing two different sloping regions rather than a sloping region followed by a plateau. This may be a function not only of the somewhat different phase and site distributions but also the different morphologies of the two materials; 8CCSO-S has a fairly large particle size and less porosity. The initial discharge and charge capacities are somewhat lower for 8CCSO-S than for 8CCSO although ICEs are similar (Table S3). The cycling performance of 8CCSO-S is also stable up to at least 100 cycles (Figure 8b). A comparison of the cycling performance of cells containing the two materials at current densities of 200 and 1 A g^{-1} appears to exhibit a similar trend (Figure S10**),** with capacities obtained for cells containing 8CCSO-S close to those of 8CCSO after 150 cycles (0.2 Ag^{-1}) and 300 cycles (1Ag^{-1}). A comparison of the 100th discharge and charge of cells containing 8CCSO and 8CCSO-S at 0.2A/g is shown in Figure S11 and reveals no significant differences (except for the somewhat lower capacity of 8CCSO-S). This suggests that the reaction products of the two materials are similar.

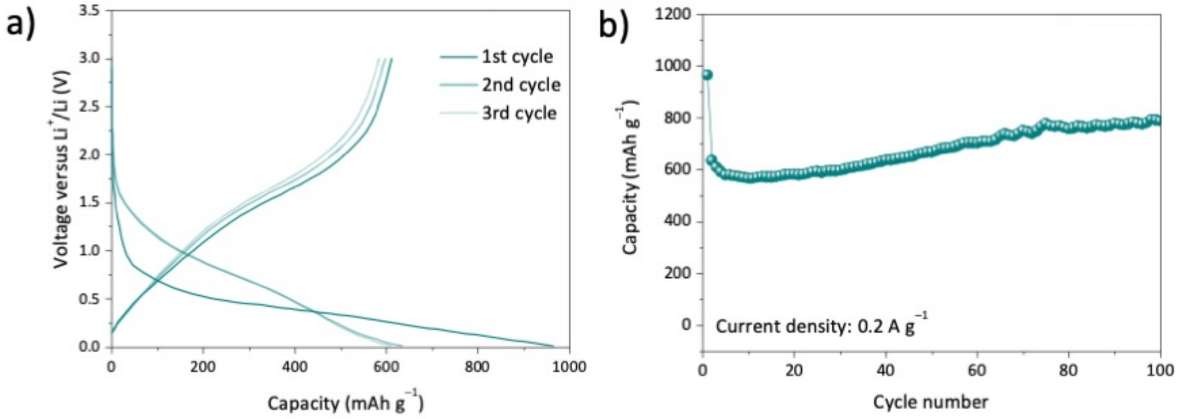

Figure 8. (a) Voltage profiles of first three cycles and b) cycling data for cells containing 8CCSO-S at 200 mAg^{-1} between 3.0-0.01V.

Somewhat surprisingly, the 2nd cycle capacity (>800 mAh/g at 0.2 Ag^{-1}) and 1st cycle coulombic efficiency (76.2%) of 5CCSO-S is significantly better than that of 5CCSO **(**Figure S12). The first discharge profile also is quite different, showing several plateaus or peaks in the dQ/dV data (Figure S12a and b), which may be a consequence of the presence of significant amounts of multiple phases with complex compositions that undergo reactions at different potentials. Figure S12c shows the second cycle at 0.2 Ag^{-1} presented in a way to show the round trip efficiency (RTE). The potential difference at the midway point is about 0.77V. The poor RTE of typical conversion anodes hinder their commercialization in battery systems and is a very difficult problem to address. While the RTE of 5CCSO-S is still higher than ideal, it appears to be somewhat better than that of the other CCSO materials. This suggests that having both phase complexity and compositional complexity may have benefits, and that it may be possible to tune materials to minimize round trip inefficiencies in conversion anode systems. However, this requires a great deal more experimentation to understand the mechanisms at play.

Lithiation/Delithiation Mechanism

To investigate the (de)lithiation mechanism of CCSOs, *ex situ* XANES analyses were performed on the initial discharge and charge, as depicted in Figure 9. For this, edge energies were compared to standards, and fittings were carried out (see experimental siection for details) to determine average oxidation states. In Figure 9a-d, the Mn in 5CCSO, 6CCSO, 7CCSO, and 8CCSO exhibit decreased energy edges after discharge in lithium half-cells, with oxidation states between Mn (II) and Mn (III) by comparison to MnO and Mn_2O_3 references. Upon cell recharge, all spectra shifted slightly toward higher energy values. For the Fe-edge (Figure 9d-h), all samples initially displayed an oxidation state of 3, characterized by similar energy edge and intensity features. Notably, in 5CCSO and 6CCSO, discharge reduced the oxidation states to near 0, when compared to the Fe foil reference. In 7CCSO and 8CCSO, the values fell between FeO and Fe_3O_4, registering as 2.4 through LCF. In the charged state, the oxidation states increased slightly to 2.8 when compared to the Fe_2O_3 and FeO references. Figure 9i-k illustrates the Co energy edge evolution for 5CCSO, 6CCSO and 7CCSO. All Co energy edges shift towards lower energy levels after lithiation, closely resembling the Co foil with an oxidation state of approximately 0. In the spectrum of the discharged 8CCSO (Figure 9l), the spectrum exhibits a higher energy edge compared to the Co foil spectra. Based on LCF, the oxidation state of Co in 8CCSO after discharge is 1.01. In the subsequent charged state, all energy edges shift slightly towards higher energy values. The Ni-edge (Figure 9m-p) for these four CCSO samples shows a consistent trend of the energy edge shifting to lower energy states during discharge, suggesting an oxidation state near Ni (0), aligning with the reference Ni foil spectrum. In the charged state, oxidation states of 5CCSO, 6CCSO, and 7CCSO remain almost the same, while charged 8CCSO returns to higher energy values with an oxidation state of 1.21. Regarding the Zn oxidation state in the 5CCSO-8CCSO samples (as depicted in Figure 9q-t), the Zn energy edges of 6CCSO, 7CCSO, and 8CCSO experience a slight shift towards lower energy levels during discharge, maintaining nearly the same energy edge after recharge. For 5CCSO, the Zn spectrum shifts toward the lower energy edge close to Zn foil at the discharged state, then reverts close to its pristine state spectrum at the charged state. Table 4 shows these results and summarizes changes in oxidation states for each of the CCSO materials upon cycling.

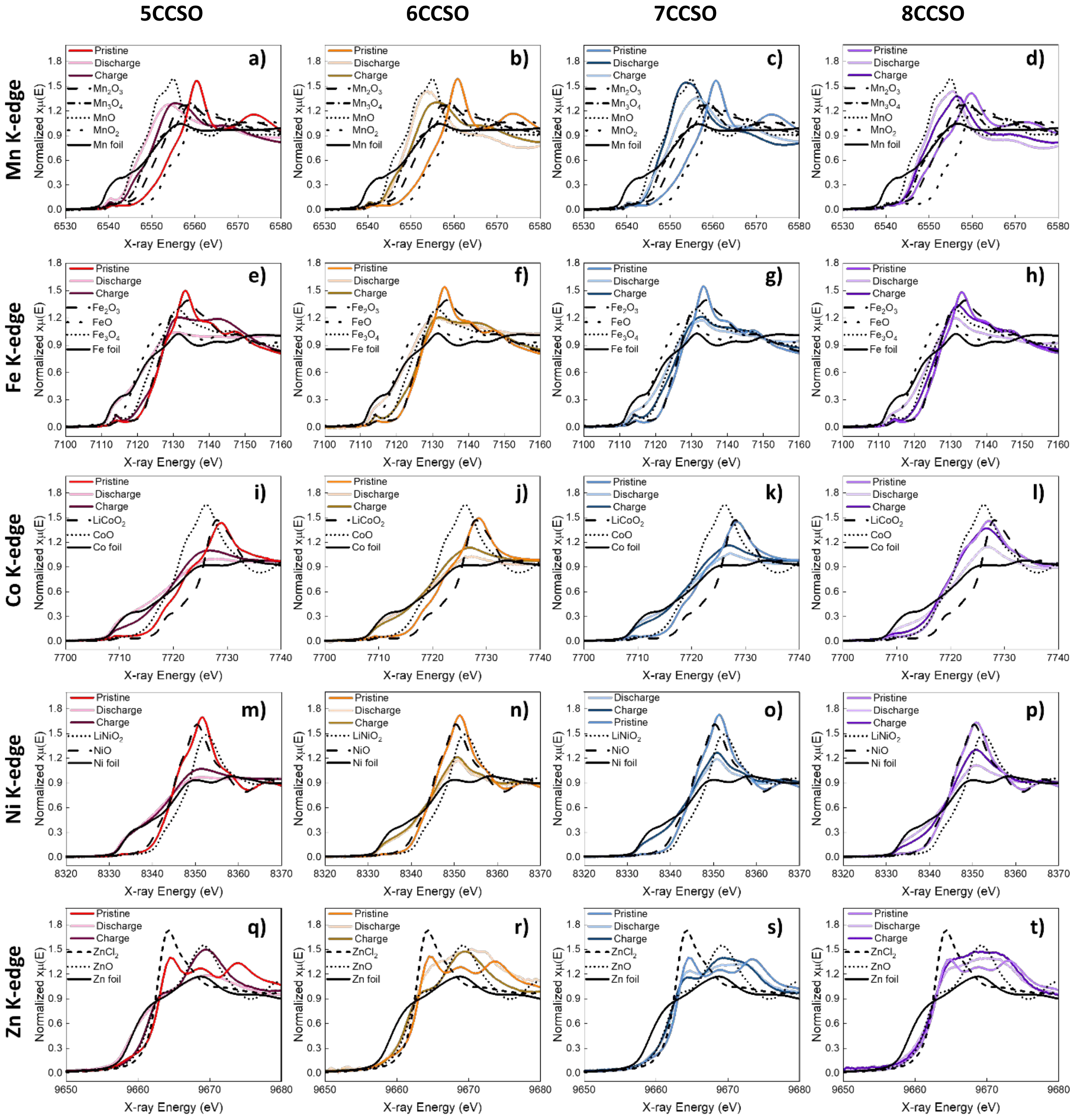

Figure 9. XANES spectra in the pristine, discharged and charged for (a, e, i, m and q) 5CCSO, (b, f, j, n and r) 6CCSO, (c, g, k, o and s) 7CCSO, and (d, h, l, p and t) 8CCSO.

Figure 10 presents alterations in oxidation states observed in each of the CCSO materials at pristine, discharged and charged states. The metallic centers of manganese (Mn) and iron (Fe) display comparatively reversible redox activity. Manganese oxidation states undergo reduction to approximately 2.1 at the initial discharged state and return to around 2.4 at the initial charged state, similar to what was found for the Mn-containing spinel ferrites. Iron oxidation states decrease notably during discharge to around 2 and increase significantly during subsequent charging to around 3. The metallic centers of Co, Ni, and Zn within the CCSO samples efficiently reduce to their metallic states of the CCSO materials in the initial discharge process. During subsequent charging, their oxidation states remained low. This suggests that the origins of the improved performance of the CCSO materials is the presence of conductive metallic components after the first discharge, similar to what was found for the spinel ferrites. However, in the case of the spinel ferrites, most of the reversible capacity derives from reduction of Fe to the metallic state followed by re-oxidation to ~+2.6 whereas iron does not reduce as far in the CCSO materials. This is a consequence of the lower iron content of the CCSOs and the increase in the content of other electroactive metals, which compensate for the lower redox activity of Fe.

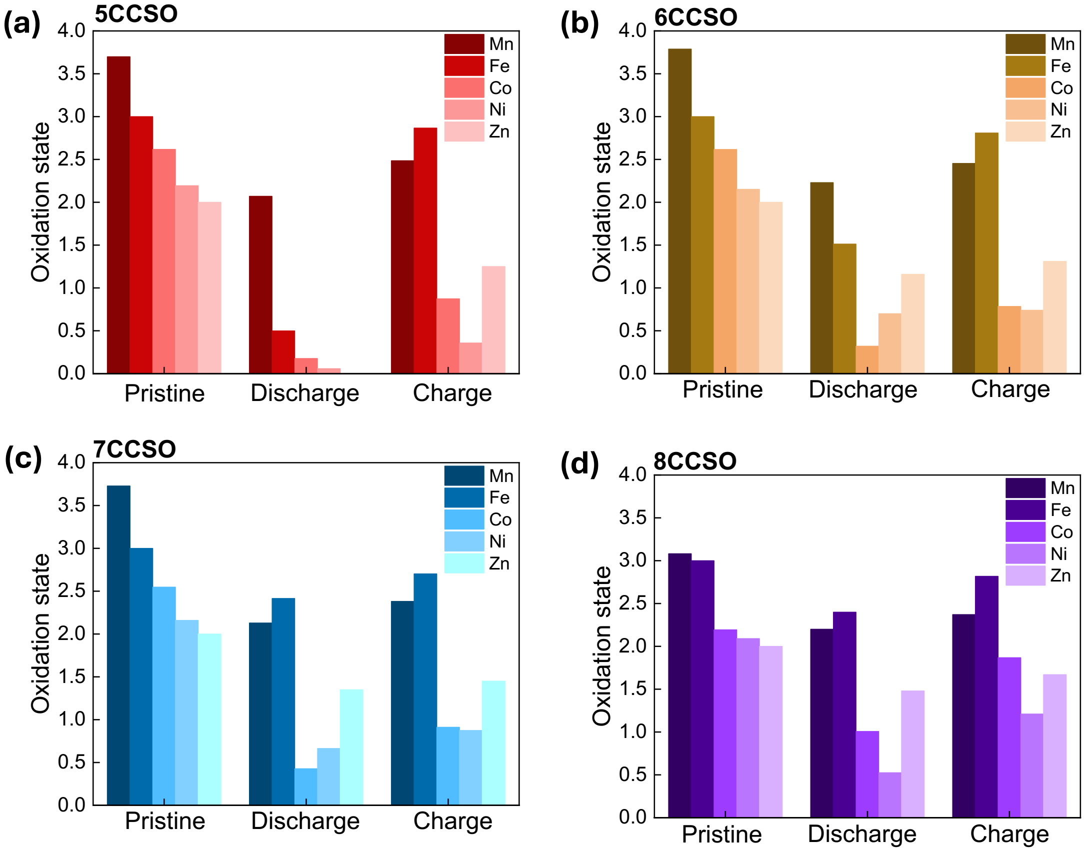

Figure 10. Oxidation state evolution of selected metals in the CCSO electrodes in the pristine state and after the first discharge and subsequent recharge: a) 5CCSO, b) 6CCSO, c)7CCSO, and d) 8CCSO.

Table 4. Oxidation states of 1st cycled high entropy spinel oxide electrode based on XANES region of XAS.

CCSO	SOC	Mn	Fe	Co	Ni	Zn
5CCSO	1st discharged	2.1	0.5	0.2	0.1	0.0
	1st charged	2.5	2.9	0.9	0.4	1.3
6CCSO	1st discharged	2.2	1.5	0.3	0.7	1.2
	1st charged	2.5	2.8	0.8	0.7	1.3
7CCSO	1st discharged	2.1	2.4	0.4	0.7	1.4
	1st charged	2.4	2.7	0.9	0.9	1.5
8CCSO	1st discharged	2.2	2.4	1.0	0.5	1.5
	1st charged	2.4	2.8	1.9	1.2	1.7
8CCSO-S	1st discharged	2.3	2.3	1.2	0.8	1.1
	1st charged	2.3	2.8	1.9	1.1	1.4

Compared with 8CCSO, 8CCSO-S shows similar oxidation state changes at the end of discharge and at end of charge for the 1st cycle (Figure 11 and Table 4). The metallic centers of manganese (Mn) and iron (Fe) exhibit relatively reversible redox activity. Iron oxidation states notably decrease during discharge to around 2 and increase significantly during subsequent charging to around 3. Cobalt oxidation states undergo reduction to approximately 1.2 at the initial discharged state and return to 1.8 at the initial charged state. The metallic centers of Mn, Ni, and Zn within the 8CCSO-S samples efficiently reduce to lower energy edges in the initial discharge process. During subsequent charging, their oxidation states remain largely unchanged.

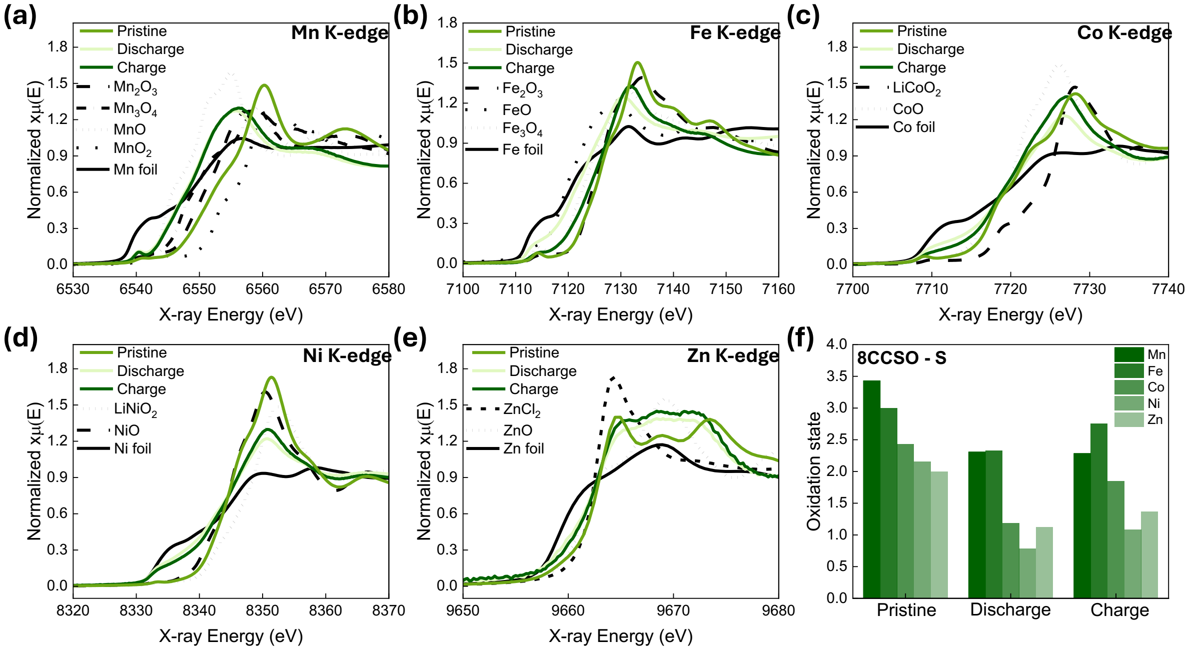

Figure 11. XANES spectra in the pristine, discharged and charged for (a-e) 8CCSO-S, and a bar chart (f) illustrates the changes in oxidation states of metals in 8CCSO-S**.**

The total contribution of Mn, Fe, Co, Ni, and Zn redox to the electrochemistry of the CCSO materials decreases as the number of components rises. There is fairly good agreement between the coulometry and the XANES experiment for cells containing 5CCSO (which contains only these 5 metals) for the initial discharge. The total number of electrons transferred, according to the XANES analysis, is 6.3 per formula unit, corresponding to about 79% of the theoretical capacity, close to the utilization of 71.7% calculated in Table S7. The XANES results considerably underestimate the utilization for 6CCSO, 7CCSO, and 8CCSO, with the discrepancies growing larger in that order. This is due, in part, to an accumulation of uncertainty in the XANES analysis as the number of components increases. However, 6CCSO, 7CCSO, and 8CCSO contain other metals (Mg, Al, Ti) that were not examined in the XANES experiments. These results strongly suggest that some or all of these metals are also reduced during the initial discharge, although the extent is unknown. This is somewhat surprising since Mg in $MgFe_2O_4$ conversion electrodes is not reduced,[11] and Ti is also difficult to reduce.[1] Other contributions to the capacity can come from alloying reactions (e.g., Mg and Al with Li), surface storage, and side reactions, as discussed previously. At any rate, the differences in behavior between these multi-component materials and simpler conversion anodes like $MgFe_2O_4$ is striking. Further investigation of these complex materials is warranted to gain an understanding of the role of each metal in determining electrochemical behavior.

Conclusions

A comprehensive physical and electrochemical investigation of oxide electrode materials containing equal amounts of 5-8 distinct metals reveals their complexity and the attendant benefits of this feature to their performance as conversion anodes. The presence of impurity phases, initial metal oxidation states, and the distributions of metals between tetrahedral and octahedral sites in the majority spinel phases in the conventionally-sized compositionally complex materials vary depending on how the materials were made and their global compositions, but all performed well electrochemically when compared to a simpler two-component $MgFe_2O_4$ that was not nanostructured. The improvement is attributed to the formation of an electronically conductive metallic network that forms upon initial cell discharge (lithiation) as certain metals are reduced and remain in a low oxidation state upon cell charge and subsequent cycling. In contrast to a related series of high entropy spinel oxide conversion anodes where iron is the majority component, XANES shows that iron is only partially reduced in most of the compositionally complex oxides in this study, which contain much less of this metal. Instead, the other metals present in the materials undergo redox, contributing to the high capacities. This indicates that the electrochemistry of the spinel oxides is a complex function of composition and not easily predicted from comparison to other known materials. The possibility of designing conversion anodes with better electrochemical properties (particularly round trip efficiencies) using complexity as a principle is posited, but will require a great deal more study to understand the role that various ions play in determining behavior.

Acknowledgments

This work was supported as part of the Center for Mesoscale Transport Properties, an Energy Frontier Research Center supported by the U.S. Department of Energy, Office of Science, Basic Energy Sciences, under award # DE-SC0012673 including the following. Work at the Molecular Foundry of Lawrence Berkeley National Lab (LBNL), was supported by the Office of Science, Office of Basic Energy Sciences of the U.S. Department of Energy under Contract No. DE-AC02-05CH11231. The research used resources of beamlines 28-ID-2 and 7-BM of the National Synchrotron Light Source II, a U.S. Department of Energy (DOE), Office of Science User Facility operated for the DOE Office of Science by Brookhaven National Laboratory under Contract No. DE-SC0012704. M.F.M. acknowledges the support of a National Science Foundation Graduate Research Fellowship Award #2234683. Any opinions, findings, and conclusions or recommendations expressed in this material are those of the authors and do not necessarily reflect the views of the National Science Foundation. E.S.T. acknowledges the William and Jane Knapp Chaired Professorship of Energy and the Environment.

Supporting Information Available

Lattice parameters of spinel and rock salt phases. SEM images of materials made by SCS. Table with theoretical and obtained capacities. EXAFS fitting results for CCSOs. XRD pattern and SEM image of 2LEO, voltage profiles during initial cycles and cycling data of half-cells containing LEO. TEM images for CCSOs made by SCS and solvothermal synthesis. Capacity as a function of cycle number for cells containing CCSOs and LEO at 0.2Ag^{-1}, comparison of cycling data at 0.2Ag^{-1} and 1Ag^{-1} of lithium half-cells containing 8CCSO and 8CCSO-S. EXAFS data and fittin parameters for 8CCSO-S and electrochemical data for 5CCSO-S.

Author Contributions

Ki-Hun Nam – materials synthesis, electrode fabrication, electrochemical cell preparation, electrochemistry and analysis, writing of initial draft.
Zhongling Wang – X-ray absorption spectroscopy analysis and writing.
Jessica Luo – X-ray diffraction refinement and writing.
Juhyeon Ahn– materials synthesis, electrode fabrication, electrochemical cell preparation, electrochemistry and analysis, writing
Zachary Mansley–HAADF/STEM experiments and writing
Seungkyu Kim-TEM data collection, writing
Myoung Hwan Oh-TEM data collection, writing
Mary Scott-TEM supervision
Armando Rodriguez Campos-Electrochemical cell preparation, sample preparation and data collection for X-ray absorption spectroscopy
Cynthia Huang – Optical emission spectroscopy data collection and analysis, X-ray absorption spectroscopy data collection.
Marie F. Millares – Optical emission spectroscopy data collection and analysis, X-ray absorption spectroscopy data collection.
Alexis Pace –Electrochemical cell preparation for ex situ XAS X-ray diffraction sample preparation and optical emission spectroscopy data collection and analysis.
Lu Ma – X-ray absorption spectroscopy support and technical input regarding data collection.
Steven Ehrlich – X-ray absorption spectroscopy support and technical input regarding data collection.

Jianming Bai – X-ray diffraction support and technical input regarding data collection.

Yimei Zhu- HAADF/STEM data collection support and technical input regarding data collection.

Esther S. Takeuchi – Interpretation characterization data, writing and editing.

Amy C. Marschilok – Interpretation characterization data, writing and editing.

Shan Yan –Sample preparation for characterization, X-ray absorption spectroscopy data collection, review of X-ray absorption spectroscopy analysis, writing.

Kenneth J. Takeuchi – defined goal of investigating spinel structured high entropy materials, interpretation characterization data comparing with prior ferrite findings, significant writing and editing.

Marca M. Doeff –design and direction of synthesis approaches, direction and interpretation of electrochemical experiments, significant writing and editing.

References

1. Cabana, J.; Monconduit, L.; Larcher, D.; Palacin, M. R., Beyond intercalation-based Li-ion batteries: the state of the art and challenges of electrode materials reacting through conversion reactions. *Adv. Mater.* **2010,** *22* (35), E170-92.
2. Bhatt, M. D.; Lee, J. Y., High capacity conversion anodes in Li-ion batteries: A review. *Internat J. of Hydrogen Energy* **2019,** *44* (21), 10852-10905.
3. Rost, C. M.; Sachet, E.; Borman, T.; Moballegh, A.; Dickey, E. C.; Hou, D.; Jones, J. L.; Curtarolo, S.; Maria, J. P., Entropy-stabilized oxides. *Nature Commun.* **2015,** *6*, 8485.
4. Sarkar, A.; Velasco, L.; Wang, D.; Wang, Q.; Talasila, G.; de Biasi, L.; Kubel, C.; Brezesinski, T.; Bhattacharya, S. S.; Hahn, H.; Breitung, B., High entropy oxides for reversible energy storage. *Nature Commun.* **2018,** *9* (1), 3400.
5. Sarkar, A.; Wang, Q.; Schiele, A.; Chellali, M. R.; Bhattacharya, S. S.; Wang, D.; Brezesinski, T.; Hahn, H.; Velasco, L.; Breitung, B., High-Entropy Oxides: Fundamental Aspects and Electrochemical Properties. *Adv. Mater.* **2019,** *31* (26), e1806236.
6. Chen, T.-Y.; Wang, S.-Y.; Kuo, C.-H.; Huang, S.-C.; Lin, M.-H.; Li, C.-H.; Chen, H.-Y. T.; Wang, C.-C.; Liao, Y.-F.; Lin, C.-C.; Chang, Y.-M.; Yeh, J.-W.; Lin, S.-J.; Chen, T.-Y.; Chen, H.-Y., In operando synchrotron X-ray studies of a novel spinel $(Ni_{0.2}Co_{0.2}Mn_{0.2}Fe_{0.2}Ti_{0.2})_3O_4$ high-entropy oxide for energy storage applications. *J. Mater. Chem. A* **2020,** *8* (41), 21756-21770.
7. Zheng, Y.; Wu, X.; Lan, X.; Hu, R., A Spinel $FeNiCrMnMgAl)_3O_4$ High Entropy Oxide as a Cycling Stable Anode Material for Li-Ion Batteries. *Processes* **2021,** *10* (1) 49.
8. Nam, K.-H.; Luo, J.; Wang, Z.; Huang, C.; Millares, M. F.; Pace, A.; Wang, L.; King, S. T.; Ma, L.; Ehrlich, S.; Bai, J.; Takeuchi, E. S.; Marschilok, A. C.; Yan, S.; Takeuchi, K. J.; Doeff, M. M., High Entropy Spinel Oxide Ferrites for Battery Applications. *Chem. Mater.* **2024**, *36* (9) 4481-4494.
9. Musicó, B.; Wright, Q.; Ward, T. Z.; Grutter, A.; Arenholz, E.; Gilbert, D.; Mandrus, D.; Keppens, V., Tunable magnetic ordering through cation selection in entropic spinel oxides. *Phys. Rev. Mater.* **2019,** *3* (10) 104416.

10. Bruck, A. M.; Brady, N. W.; Lininger, C. N.; Bock, D. C.; Brady, A. B.; Tallman, K. R.; Quilty, C. D.; Takeuchi, K. J.; Takeuchi, E. S.; West, A. C.; Marschilok, A. C., Temporally and Spatially Resolved Visualization of Electrochemical Conversion: Monitoring Phase Distribution During Lithiation of Magnetite (Fe_3O_4) Electrodes. *ACS Appl. Energy Mater.* **2019,** *2* (4), 2561-2569.

11. Bock, D. C.; Tallman, K. R.; Guo, H.; Quilty, C.; Yan, S.; Smith, P. F.; Zhang, B.; Lutz, D. M.; McCarthy, A. H.; Huie, M. M.; Burnett, V.; Bruck, A. M.; Marschilok, A. C.; Takeuchi, E. S.; Liu, P.; Takeuchi, K. J., (De)lithiation of spinel ferrites Fe_3O_4, $MgFe_2O_4$, and $ZnFe_2O_4$: a combined spectroscopic, diffraction and theory study. *Phys. Chem. Chem. Phys. : PCCP* **2020,** *22* (45), 26200-26215.

12. Chick, L. A. P., L.R.; Maupin, G.D.; Bates, J. L.; Thomas, L.E.; Exarhos, G. J., Glycine-nitrate combustion synthesis of oxide ceramic powders. *Mater. Lett.* **1990,** *10*, 6-12.

13. Toby, B. H.; Von Dreele, R. B., GSAS-II: the genesis of a modern open-source all purpose crystallography software package. *J. Appl. Crystal.* **2013,** *46* (2), 544-549.

14. Ravel, B.; Newville, M., ATHENA, ARTEMIS, HEPHAESTUS: data analysis for X-ray absorption spectroscopy using IFEFFIT. *J. Synchrotron Radiat* **2005,** *12* (4), 537-541.

15. Dau, H.; Liebisch, P.; Haumann, M., X-ray absorption spectroscopy to analyze nuclear geometry and electronic structure of biological metal centers—potential and questions examined with special focus on the tetra-nuclear manganese complex of oxygenic photosynthesis. *Anal. and Bioanal. Chem.* **2003,** *376*, 562-583.

16. Brahlek, M.; Gazda, M.; Keppens, V.; Mazza, A. R.; McCormack, S. J.; Mielewczyk-Gryń, A.; Musico, B.; Page, K.; Rost, C. M.; Sinnott, S. B.; Toher, C.; Ward, T. Z.; Yamamoto, A., What is in a name: Defining "high entropy" oxides. *APL Materials* **2022,** *10* (11) 110902.

17. Dippo, O. F.; Vecchio, K. S., A universal configurational entropy metric for high-entropy materials. *Scripta Materialia* **2021,** *201* 113974.

18. Fumo, D. A.; Jurado, J. R.; Segadaes, A. M.; Frade, J. R., Combustion Synthesis of Iron-Substituted Strontium Titanate Perovskites. *Mater. Res. Bull.* **1997,** *32* (10), 1459-1470.

19. Dong, L.; Wang, Z.; Li, Y.; Jin, C.; Dong, F.; Zhao, W.; Qin, C.; Wang, Z., Spinel-Structured, Multi-Component Transition Metal Oxide $(Ni,Co,Mn)Fe_2O_{4-x}$ as Long-Life Lithium-Ion Battery Anode Material. *Batteries* **2023,** *9* (1).

20. Shirpour, M.; Cabana, J.; Doeff, M., New materials based on a layered sodium titanate for dual electrochemical Na and Li intercalation systems. *Energy & Environ. Sci.* **2013,** *6* (8), 2538-2547.

21. Sivakumar, N.; Gnanakan, S. R. P.; Karthikeyan, K.; Amaresh, S.; Yoon, W. S.; Park, G. J.; Lee, Y. S., Nanostructured $MgFe_2O_4$ as anode materials for lithium-ion batteries. *J. Alloys and Compounds* **2011,** *509* (25), 7038-7041.

22. Keppeler, M.; Srinivasan, M., Interfacial Phenomena/Capacities Beyond Conversion Reaction Occurring in Nano-sized Transition-Metal-Oxide-Based Negative Electrodes in Lithium-Ion Batteries: A Review. *ChemElectroChem* **2017,** *4* (11), 2727-2754.

Table of Contents Graphic